

## Ti6Al4V functionally graded material via high power and high speed laser surface modification

Yaoyi Geng, Éanna McCarthy, Dermot Brabazon, Noel Harrison

<sup>a</sup> Mechanical Engineering, National University of Ireland Galway, Ireland

<sup>b</sup> I-Form Advanced Manufacturing Research Centre, Ireland

<sup>c</sup> Ryan Institute for Environmental, Marine and Energy Research, NUI Galway, Ireland

<sup>d</sup> IComp Irish Composites Centre, Ireland

<sup>e</sup> Centre for Marine and Renewable Energy Ireland, Galway, Ireland

<sup>f</sup> Advanced Processing Technology Centre, Dublin City University, Ireland

Corresponding Author: [y.geng1@nuigalway.ie](mailto:y.geng1@nuigalway.ie)

### Abstract

This study investigates the fabrication of Ti6Al4V functionally graded material via high power and high speed laser surface modification (LSM). The original sample microstructures consisted of elongated equiaxed  $\alpha$  phase with a grain boundary of  $\beta$  phase. Nine different LSM process parameter sets were applied to these samples. Scanning electron microscopy showed a fine acicular martensitic phase next to the surface of the laser treated samples in all cases. A transition microstructure zone beneath the martensitic zone was observed, with larger, equiaxed grains and some martensitic  $\alpha$  phase growth. The interior of the sample contained the original microstructure. The surface roughness was found to increase after the surface modification for all process parameter sets. Nanoindentation tests were performed in order to obtain the hardness and modulus of the three phases, i.e. martensitic  $\alpha$ , equiaxed  $\alpha$  and the grain boundary  $\beta$ . A dual phase crystal plasticity finite element model was developed to investigate the three zone functionally graded microstructure under uniaxial tensile loading. The hardened surface zone prevented the propagation of continuous slip bands, while the transition zone prevented excessively sharp stress concentrations between the outer surface and interior of the samples.

### Keywords

Functionally graded material, Laser surface modification, Ti6Al4V, Crystal plasticity finite element Nanoindentation

To cite this article: Yaoyi Geng, Éanna McCarthy, Dermot Brabazon, Noel Harrison, *Ti6Al4V functionally graded material via high power and high speed laser surface modification*, *Surface & Coatings Technology* 398 (2020) 126085.

## 1. Introduction

Functionally graded materials (FGMs) refer to materials which have been engineered to have adjacent locally modified properties of a material which could otherwise be homogeneous. They have been categorized into surface coating FGM and bulk FGM associated with the thickness of the gradient of the material properties [1]. Bulk FGMs have attracted much attention from researchers in many engineering fields, including aerospace engineering, marine engineering, orthopaedic devices and dental implants [2,3]. However, changing the properties of the entire sample dramatically increases the fabrication time [4]. There are limited processes available for fabrication of bulk FGM components and they tend to be inefficient in terms of both time and energy required for modifying local properties of the entire sample. Therefore, surface (only) modification has emerged as a more readily attainable FGM category. Surface FGMs offer a new approach to component and process design with gradient in microstructure and mechanical properties confined to a thin layer on the surface, thus facilitating a high productivity rate via rapid surface processing.

Mechanical surface treatment FGM fabrication methods have been extensively applied in metals. For example, severe surface deformation has been applied to produce a surface-to-interior microstructure gradient with a nanoscale gradient grain size with a depth of 150  $\mu\text{m}$  in steel [5] and copper [6]. Shot peened FGM with optimized microstructural gradation has shown improvements in fretting resistance in Ti6Al4V and SiCp/2024Al [7,8]. Surface work-hardening has produced an improvement in strength and ductility via micro-scale gradient Cu with nano-grains on the surface and normal grains in the centre of the material [9]. In addition, chemical and thermomechanical methods such as nitriding [10] have been demonstrated for surface FGM manufacturing.

Laser surface modification (LSM) is a unique surface treatment method, where a heat source is rapidly applied on the surface of the material, and can be set to cause temporary partial surface melting. The resultant microstructure is largely determined by the cooling rate during the solidification and solid phase transformation. In addition, a region near the surface, called the transition zone or heat affected zone is generated in the material. The thickness and the chemical composition [11] of the transition zone is closely related to the thermal history of the laser. Thus, the purpose of LSM is to retain the key bulk properties of the material while the modified surface can lead to improved mechanical properties such as hardness, corrosion resistance and biocompatibility [4].

Ti6Al4V is a dual phase titanium alloy, which is the work horse of titanium alloys used in industry due to its high strength to weight ratio and favorable surface properties such as high corrosion resistance and good biocompatibility [12]. Ti6Al4V has been extensively used in aerospace, biomedical, and high-performance sports applications since its invention in 1954. The literature contains extensive research on the microstructure [13,14], fatigue and fretting performance [15,16], and other tribology properties [17,18] of Ti6Al4V.

LSM has been conducted on dual phase titanium alloys to improve its surface hardness and modulus [13,14,19]. The hardening mechanism has been explained by the ultra-fine acicular grained layer at the surface thanks to the high solidification rate [20]. LSM also improves wear and fatigue properties. Previous studies have also reported the improved hardness and fatigue life of Ti6Al4V [10] and Ti5Al2.5Sn [21] by LSM. This process has also been used to improve the tribology performance of Ti6Al4V [18,22], where LSM process parameters (laser power and travel speed) were shown to directly influence FGM depth and resulting wear properties [23]. Studies by Brabazon's group [11,24,25] have produced a thin layer of martensitic surface of the thickness between 20  $\mu\text{m}$  and 50  $\mu\text{m}$  on the Ti6Al4V samples without initiating cracks. In addition to the mechanical properties, LSM has improved surface biocompatibility and wettability of orthopaedic implants to promote early stage cell attachment [3]. For these reasons, LSM has become established within the medical device industry such as knee and hip joint implants to improve service life [17].

Crystal plasticity finite element (CPFE) model is a powerful computational tool to predict the response of metals at the microscale. The method considers polycrystalline structures by defining grain morphology, grain orientation and lattice slip systems. It has been used to predict the inter- and intra-granular mechanical behaviour of single grains [26,27] and polycrystalline materials [28,29]. The CPFE method has been applied in the dual phase Ti6Al4V in uniaxial tensile test, fatigue [30] and fretting [16,31]. CPFE toolkits have been developed such as Huang's single crystalline model [32], the DAMASK toolkit [33,34] and the PRISMS-Plasticity package [32,35].

Laser treatment has been shown to significantly improve the mechanical properties of the Ti6Al4V sample including the yield strength [36,37]. However, the grain scale hardening mechanism has not been sufficiently studied, nor was the transition zone of the microstructure systematically investigated. Possible mechanisms for this include the prevention of slip band propagation due to increased grain boundary and stress concentrations between the outer and interior of the sample. Previous studies have focused on the overall performance of the treated samples. This is partly because the surface layer is hard to observe, due to the shallow nature of the laser penetration depth. In this study, high laser power and sample moving speed were optimized, in order to obtain thick FGM surface allowing identification and characterisation of distinct zones of the microstructure evolution along the laser processed region. CPFE modelling was then used to characterise the mechanical performance of the resultant structures, in comparison to the original non-FGM material.

## 2. Material and methods

### 2.1. Laser surface modification

The material used in the current study is flat annealed Ti6Al4V from Super Alloys International Limited (Milton Keynes, UK). The chemical composition of the material is shown in Table 1. The two rectangle samples are of the dimensions of 5 mm thickness, 20 mm width and 90 mm length. The original (pre-LSM) microstructure consists of  $\alpha$  and  $\beta$  phases (see in Section 3.2). The samples were sandblasted before laser treatment for better laser absorption using a Guyson Formula 1400 blaster with soda lime glass (spherical particles with a particle size of 106  $\mu\text{m}$  to 212  $\mu\text{m}$  and a Mohs hardness of 5) at 8 bar. The samples were LSM treated using a Rofin DC 015 industrial CO<sub>2</sub> laser at the Advanced Processing Technology Centre, Dublin City University (APT, DCU, see Fig. 1) as previous used by Chikarakara et al. [11,24,25]. The laser has a wavelength of 10.60  $\mu\text{m}$  and a spot size of 200  $\mu\text{m}$ . All laser treatments were operated in continuous mode under 2 bar Argon assist gas. A 10 mm by 20 mm area was laser treated for each parameter set, and the treated surface was sectioned along the width of the sample. As shown in Fig. 2, the laser moved along the sample width with 30% overlap. Three laser power and three sample travel speed settings were used, leading to a total of nine process parameter sets as detailed in Table 2.

Table 1. Chemical composition of the Ti6Al4V used in the presented study.

Element	Ti	Al	V	O	Fe	C	Si
wt%	Bal.	6.36	3.97	0.17	0.16	0.14	0.01

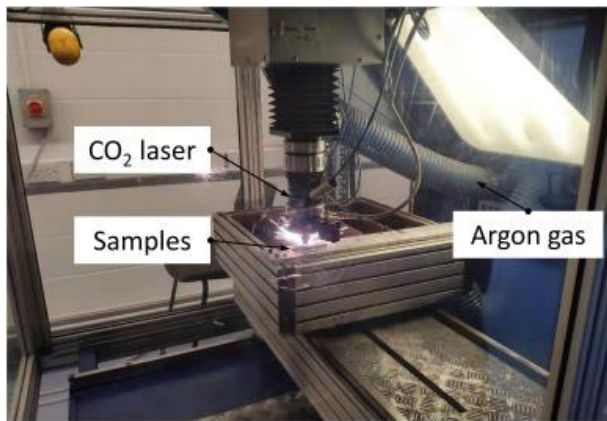


Fig. 1. Rofin DC 015 industrial CO2 laser setup used in the present study.

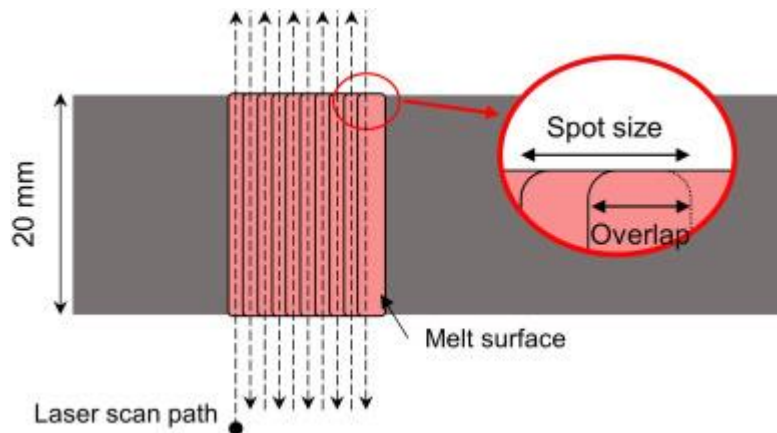


Fig. 2. Top view of the laser path and inset showing laser spot overlap produced during the surface treatment.

**Table 2**  
Laser parameters used for each parameter set.

Parameter ID	Laser power (W)	Sample speed (mm/s)	Energy density (J/mm <sup>2</sup> )
1	222	83.33	33
2	300	83.33	44
3	378	83.33	58
4	222	66.20	23
5	300	66.20	29
6	378	66.20	38
7	378	54.93	17
8	300	54.93	22
9	222	54.93	29

## 2.2. Surface roughness

The surface roughness of laser treated samples was measured using a Keyence VHX2000E 3D digital microscope at Nanobioanalytical Research Facility, Dublin City University (NRF, DCU) with a 500× magnification. 3D images of 1500 μm length by 1240 μm width surface area at the centre of each treated surfaces with a resolution of 2.0 μm were obtained and used to calculate the surface roughness. The

average arithmetical mean height Ra was calculated using the height profile from four edges and two diagonals on each 3D height profile.

### 2.3. Electron microscopy

After LSM processing, the samples were sectioned using Metacut-M251 Manual Cut Off Machine, water cooled. They were mounted with Aka-Resin liquid epoxy and Aka-Cure Quick 500 (AKASEL, Roskilde, Denmark). The samples were initially polished with P320 sandpaper to remove the thermal effect area from the cutting process. The obtained cross section was then polished with P600, P800 and P1200 sandpaper, followed by UltraPad (Buehler, Illinois, USA) with 9 Supreme Diamond fine polish. Final polish was carried out using ChemoMet (Buehler, Illinois, USA) and 0.054 mm colloidal silica (MetPret Ltd. Coventry, UK). The samples were etched with Kroll's reagent (2% HF, 6% HNO<sub>3</sub>, 92% water) for 15 s and cleaned in acetone in an ultrasonic bath. Scan electron microscope (SEM) images were taken with a Jeol JSM-IT 100 InTouchScope electron microscope at NRF, DCU. The images were obtained at an accelerating voltage of 10 kV (high vacuum mode) with a spot size 50  $\mu\text{m}$ .

### 2.4. Nanoindentation

Nanoindentation was carried out using a Bruker HYSITRON TI Premier nanoindenter with a Berkovich tip at NRF, DCU. Nine indents were performed on the martensitic surface. Eight indents were performed on the equiaxed  $\alpha$  and grain boundary (GB)  $\beta$  in the centre of the sample, respectively. Although it has been shown that the maximum load effects measured hardness and modulus results, nanoindentation is an effective method to measure the elastic modulus [38,39]. For all indents performed, the maximum load was 1000  $\mu\text{N}$  (load control), holding time at maximum stress was 2 s, loading and unloading rate was 200  $\mu\text{N/s}$ .

### 2.5. Crystal plasticity finite element model

A CPFE model was generated of the surface FGM zones incorporating a dual-phase phenomenological constitutive model for Ti6Al4V as described in [40] and Appendix II. Body centred cubic (BCC) and hexagonal close packed (HCP) lattice structures were employed to capture the different slip systems in dual phase Ti6Al4V. The slip systems used in the model are detailed in Table 3.

Table 3. Slip systems used in the crystal plasticity model in the two phases.

Lattice type	Slip type	Slip system	Number of slip systems
HCP	Basal	(0001) $\langle 11\bar{2}0 \rangle$	3
HCP	Prismatic	(00 $\bar{1}$ 0) $\langle 11\bar{2}0 \rangle$	3
HCP	Pyramidal	(00 $\bar{1}$ 1) $\langle 11\bar{2}3 \rangle$	12
BCC	–	(110) $\langle 111 \rangle$	12

The laser treated microstructure is complex and would be computational expensive if directly imported into the finite element solver. In the CPFE study, the microstructure is simplified into three zones. The surface layer is assumed to be perfect columnar microstructure with  $\alpha$  and  $\beta$  laths between each other. The transition zone under the surface layer is simplified into equiaxed  $\alpha$  grains with  $\beta$  laths within these grains. The original microstructure was represented with equiaxed grains. The 2D grain morphology for a 100  $\mu\text{m} \times 240 \mu\text{m}$  sample size was generated using Voronoi Tessellation to produce a microstructure with statistically equivalent to the grain size estimated based on Section 3.2. The equiaxed grains were generated using Rhinoceros® CAD (Robert McNeel & Associates, WA, USA) and the Grasshopper® plugin as detailed in the existing study [40]. The surface the transition zone was then sectioned into lath in Abaqus using Python script with the desired lath thickness. The surface roughness of the sample was not considered in the current study. A control group with the original

equiaxed microstructure was studied is shown in Fig. 3a using the same average grain size as the FGM model and sample dimensions. The surface treated microstructure is shown schematically in Fig. 3b. The original microstructure is elongated equiaxed microstructure with  $\alpha$  grains surrounded by grain boundary (GB)  $\beta$ . Some computational studies have included explicit representation of the grain boundaries in smaller sample sizes [41]. However, the current study requires a larger sample size, thus limiting grain boundary definition to zero-thickness linear boundaries due to computational costs. In the current study, the primary interest lies in the surface layer thus the GB  $\beta$  phase at the centre of the sample was neglected.

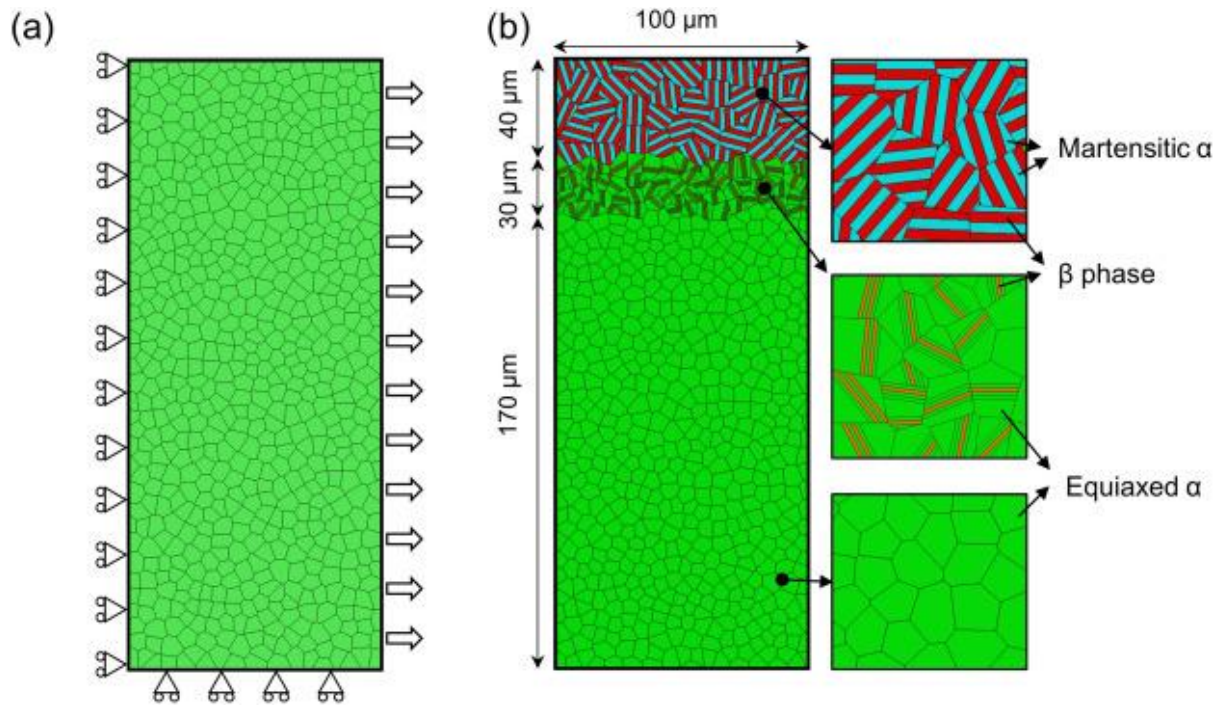


Fig. 3. CPFE model from Abaqus in the current study (a) original microstructure (b) LSM microstructure.

**Table 4**

Parameter adopted in the current study obtained from nanoindentation test and Geng et al. [40].

Equiaxed $\alpha$		
Elastic modulus, $E$ (MPa)	Poisson's ratio, $\nu$	Hardening parameters (MPa)
129,970	0.46	$h_0 = 1034, h_x = 35, \tau_x = 48,$
Strain rate sensitivity, $m$	Latent hardening factor, $q$	$\tau_0 = 296$
50	1.4	
Martensitic $\alpha$		
Elastic modulus, $E$ (MPa)	Poisson's ratio, $\nu$	Hardening parameters (MPa)
133,570	0.46	$h_0 = 1034, h_x = 35, \tau_x = 48,$
Strain rate sensitivity, $m$	Latent hardening factor, $q$	$\tau_0 = 296$
50	1.4	
$\beta$ phase		
Elastic modulus, $E$ (MPa)	Poisson's ratio, $\nu$	Hardening parameters (MPa)
64,170	0.46	$h_0 = 3068, h_x = 37, \tau_x = 53,$
Strain rate sensitivity, $m$	Latent hardening factor, $q$	$\tau_0 = 498$
50	1.4	

An average grain size of 5  $\mu\text{m}$  was used in the centre of the material. The transition zone has a thickness of 30  $\mu\text{m}$ , which consists of equiaxed microstructure and newly formed laths within the original equiaxed grains. The lath thickness of the transition zone was set to be 0.5  $\mu\text{m}$ . The outermost layer exhibits needle shaped martensitic microstructures. The surface layer has a thickness of 40  $\mu\text{m}$ . The grains were sectioned into  $\alpha$  and  $\beta$  laths. The lath thickness at the surface layer was adopted from the SEM (see Fig. 6 in Section 3.2) images as 2.0  $\mu\text{m}$ . The elastic moduli utilised in the CPFEM model were obtained from the nanoindentation test and other mechanical properties detailed in Table 4 were adopted from a previous study [40].

Table 4. Parameter adopted in the current study obtained from nanoindentation test and Geng et al. [40].

In order to predict the mechanical behaviour of FGM microstructure under a uniaxial tensile test, the plate was loaded in tension horizontally on the right edge with a displacement of 1.5  $\mu\text{m}$ . The left edge is constrained in the horizontal direction. The bottom edge is constrained with a symmetric boundary condition, and the upper edge is unconstrained. The same boundary conditions were applied to both the original microstructure and the SLM microstructure. Linear quadrilateral elements (Abaqus element type: CPS4) was used throughout the study. The global mesh size of 0.5  $\mu\text{m}$  was applied and a total of 112,843 and 112,489 elements were used in the original and laser treated models, respectively, following mesh convergence studies.

### 3. Results

#### 3.1. Surface roughness

The average arithmetical mean height  $R_a$  is shown in Fig. 4. Compare to the previous study [25], the high speed and laser power results in an increased surface roughness. Low laser power (sample ID: 1, 4, 9) was found to result in lower surface roughness. Scan speed has little effect on the surface roughness. The highest surface roughness was found when using a laser power of 300 W and a sample travel speed of 54.93 mm/s.

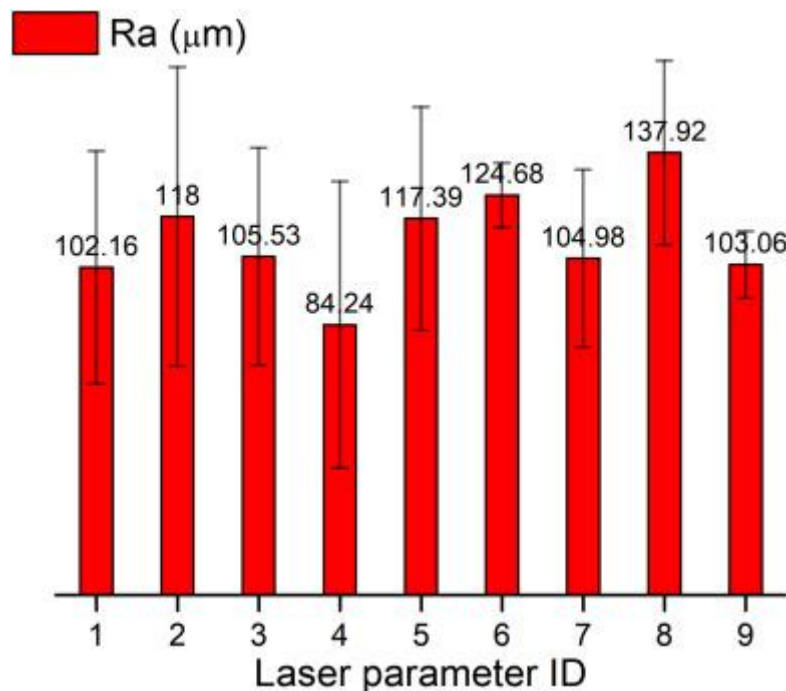


Fig. 4. Average arithmetical mean height  $R_a$  of the nine laser treated surfaces (error bars indicate the standard deviation).

### 3.2. Electron microscope

SEM micrographs of the border between the re-solidified melt pool and the transition zone for each parameter combination are shown in Fig. 5. With a laser power range from 222 W to 378 W and a sample travel speed range from 54.93 mm/s to 83.88 mm/s, the laser treated surface zone exhibits an acicular martensitic phase due to high cooling rate in the melt pool. In all parameter sets, the surface layer microstructures were altered by the rapid heating and cooling and a martensitic layer as well as a transition layer were observed. The thickest transition zone was obtained with a laser power of 300 W and speed of 66.20 mm/s. It is noteworthy that the heat affected zones under the melt pools seems blurred (Fig. 6a, c). The view is not out of focus - this indicates that the grain boundaries are partially decomposed and therefore the grain boundaries start to disappear. Compared with the previous work conducted by Chikarakara et al. [25], the current study used a higher laser power and range of speeds. The high laser power results in a greater laser penetration depth, but at the cost of a high surface roughness.

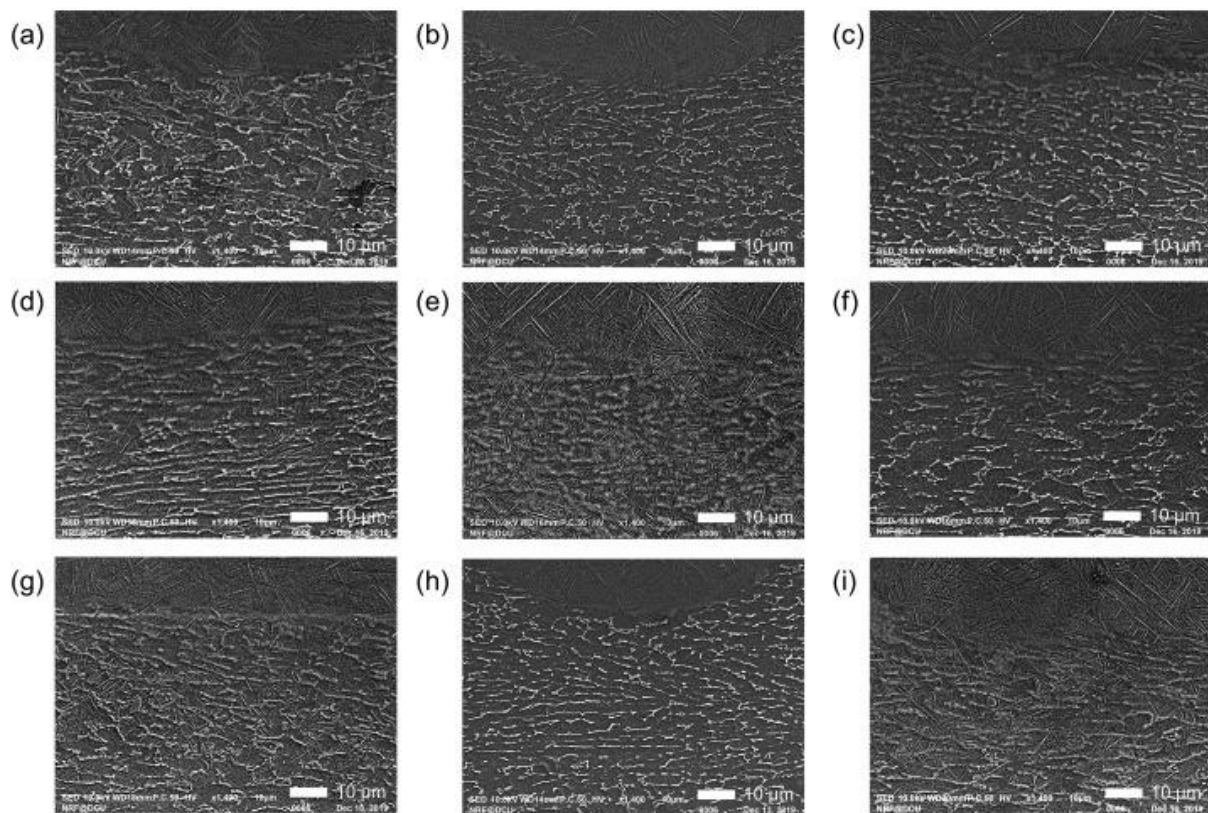


Fig. 5. The microstructure of the boundary between the melt pool (shown at the top of the images) and the transition zone beneath this for the samples processed with laser parameters ID 01 (a) to ID 09 (i).

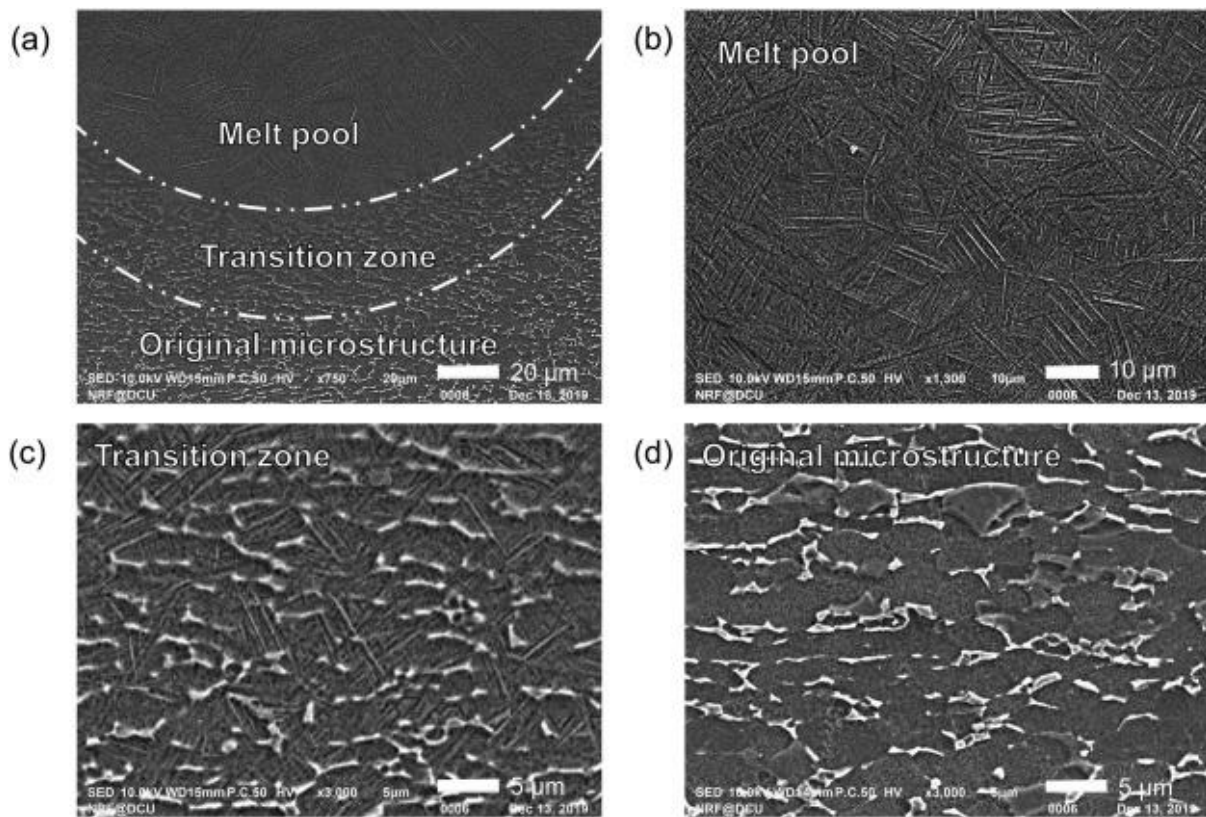


Fig. 6. Laser treated surface of sample ID 05, 300 W, 66.20 mm/s (a) three-stage microstructure evolution (b) within the melt pool (c) transition zone (d) original microstructure.

To understand the microstructure transition, magnified microstructures of the region beneath the melt pool for sample ID 05 are shown in Fig. 6. The original microstructure of the samples were elongated equiaxed  $\alpha$  with grain boundary  $\beta$  (Fig. 6b). Within the melt pool, needle martensitic  $\alpha$  was observed with a  $\beta$  substrate. Beneath the melt pool, a transition area was observed as is shown in Fig. 6c. The original grain boundaries are partially melted, and martensitic lamellar  $\alpha$  phases within each equiaxed grain have grown. The original equiaxed microstructure remains under the transition zone (Fig. 6d).

### 3.3. Nanoindentation

Indentation on single grains has been investigated both experimentally [42] and computationally [43]. The in-situ scanning probe microscopy image from the nanoindenter is shown in Fig. 7. Due to the difference in stiffness, the two phases exhibited different topology features. Therefore, indents were performed on the two regions with distinguishable stiffness values as in Fig. 7. Indentation locations from 0 to 7 was the grain boundary  $\beta$ , and locations from 8 to 15 were equiaxed  $\alpha$ . The load-displacement curve on the three identified zone phase structures is shown in Fig. 8. Indents performed on the  $\beta$  phase show the highest maximum displacement, which indicates the lowest hardness. Indents on the martensitic  $\alpha$  phase showed that this phase presented the highest hardness. There is a relative high deviation in the measured elastic modulus in the  $\beta$  phase, mainly due to the thin  $\beta$  grains and the interaction between the equiaxed  $\alpha$  grains. The average hardness and reduced modulus were calculated from the loading curves as shown in Fig. 9. The modulus values were used in the CPFPE model presented in Section 3.4.

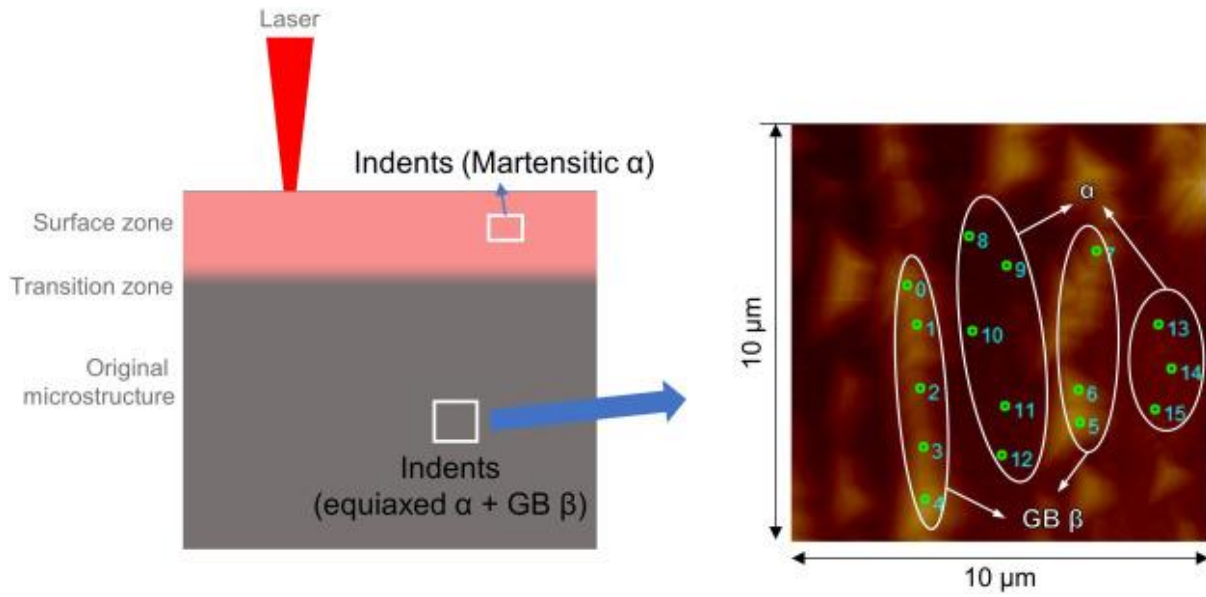


Fig. 7. Indentation locations on the sample cross section (left) and in-situ scanning probe microscopy showing indentation locations GB  $\beta$  and equiaxed  $\alpha$  (right).

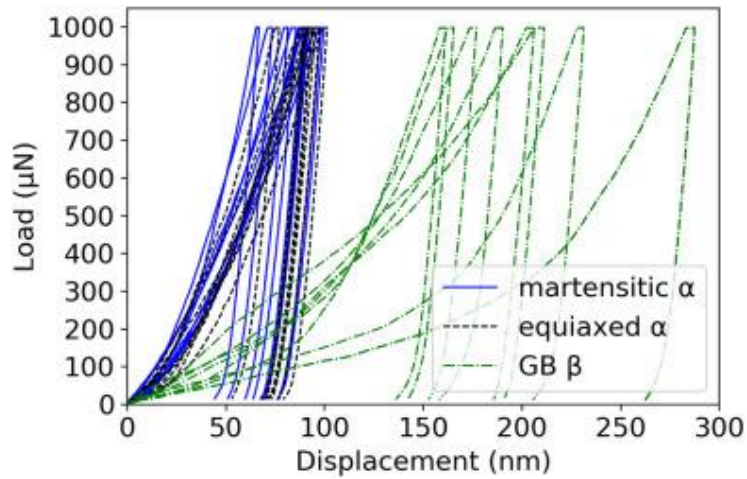


Fig. 8. Load-displacement curve from nanoindentation on the three phases.

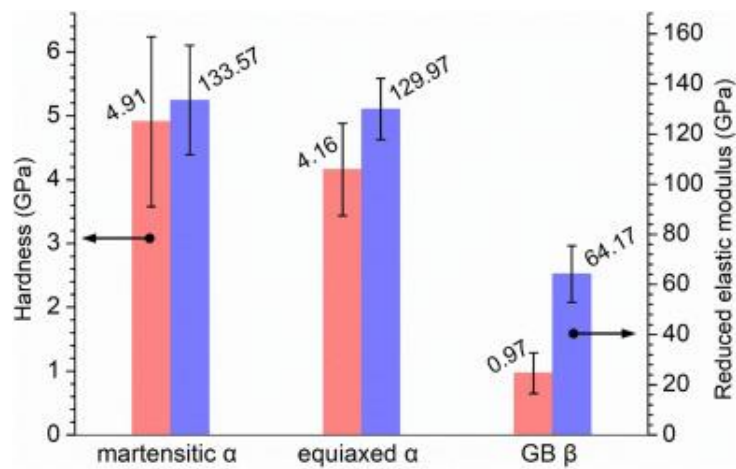


Fig. 9. Reduced modulus and hardness of the martensitic  $\alpha$ , equiaxed  $\alpha$  and GB  $\beta$  phase from nanoindentation.

### 3.4. Crystal plasticity finite element model

The Von Mises stress of both microstructures was plotted in Fig. 10 to evaluate the equivalent stress state. In the SLM sample, high stress field was observed at the surface layer followed by the transition layer. High stress can be observed at the grain boundaries in the surface layer. While at the centre of the material, the equiaxed grains show lower stress. Stress concentration at the surface was observed, which is a result of grain boundary hardening in the martensitic microstructure. The stress distribution in the original microstructure (Fig. 10a) shows no gradient from the centre to the surface.

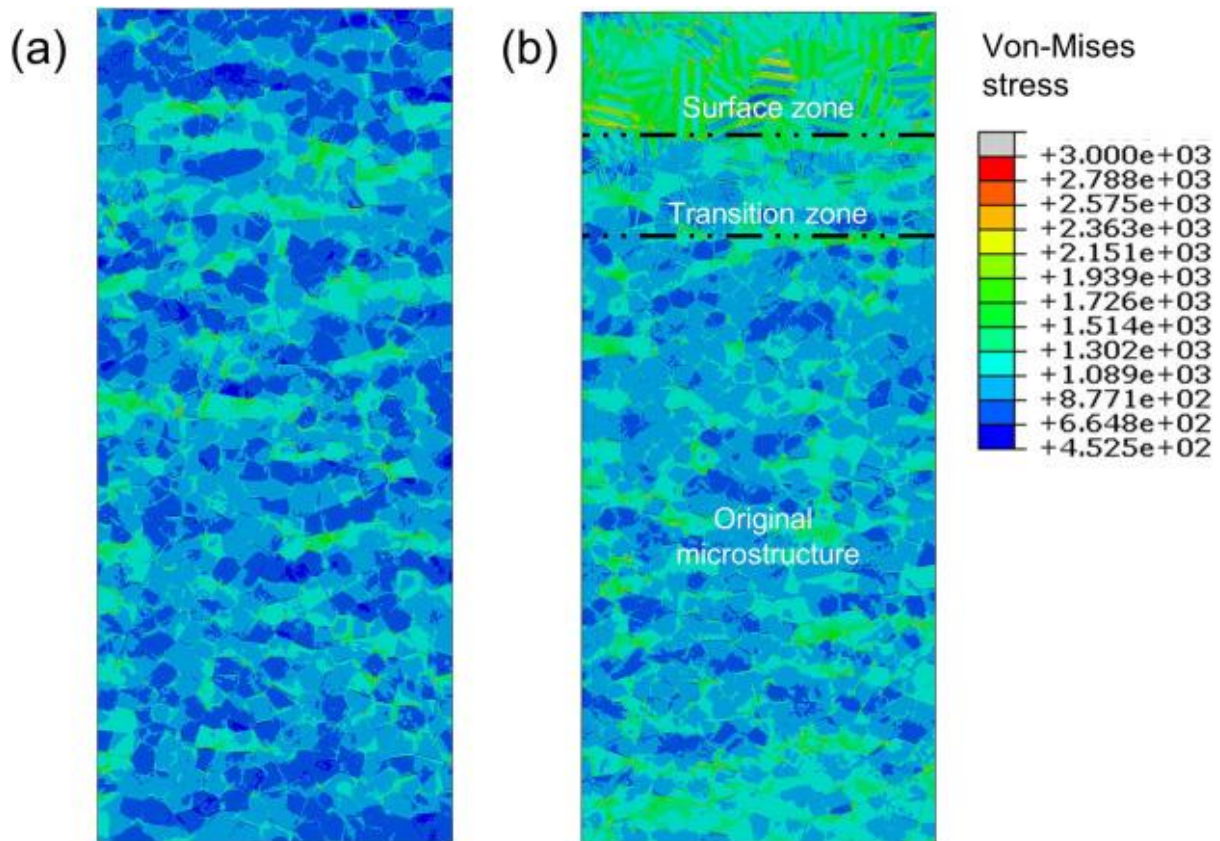


Fig. 10. Contour plot of Von Mises stress (unit: MPa) in (a) original microstructure and (b) laser treated FGM.

The principle in-plane strain was analysed in this study to evaluate the deformation of the 2D model. The maximum logarithm strain of the original and laser modified microstructures were plotted in Fig. 11. In the original microstructure, continuous slip bands were observed. While in the laser treated microstructure, the 45-degree aligned high stress bands in the non-modified centre zone gradually disappear toward the martensitic surface layer. Therefore, the hardened surface with high modulus and hardness limited the formation of continuous deformation bands of the sample (Fig. 11).

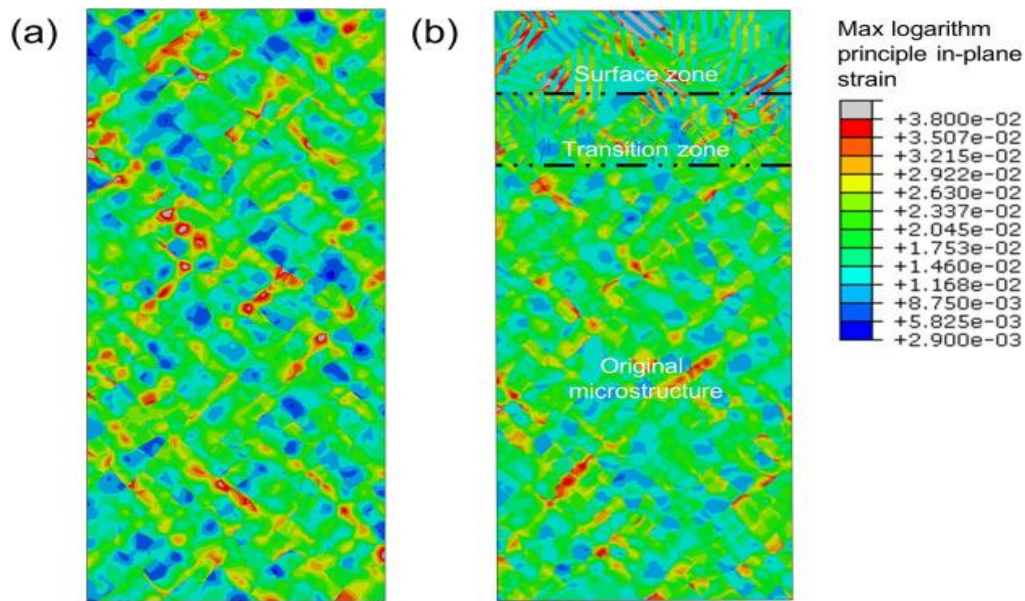


Fig. 11. Contour plot of maximum logarithm principle in-plane strain in the (a) original and (b) laser treated FGM microstructures.

## 4. Discussion

### 4.1. Formation of three zone microstructure

LSM has been extensively investigated with titanium alloys to improve the biocompatibility and the mechanical properties, including hardness and elastic modulus [3]. The hardening effect of the surface modification is resulted by a surface melting and cooling process. The high power and rapid cooling of a laser treatment on the surface enables a thin surface layer to melt and solidify in milliseconds. A modified surface layer of the thickness of the depth of approximately equal to the melt pool was generated, surrounded by a heat affected zone.

The rapid laser heat input results in a thermal gradient within the melt pool. This is depicted in Fig. 12. Needle shaped martensitic  $\alpha$  phase was formed due to the extremely high thermal gradient and cooling rate. In the transition zone, the cooling rate was lower and causes the original grain boundaries  $\beta$  to decomposes and results in needle martensitic  $\alpha$  phase nucleation. However, the lower cooling rate (compared with the melt pool) allows the laths to grow within the grains [44,45].

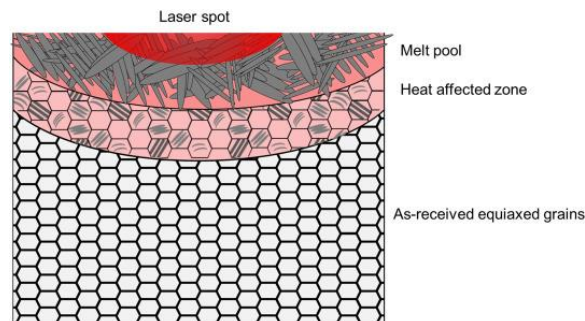


Fig. 12. Schematic image of the formation of the three zone functionally graded microstructure.

### 4.2. Influence of LSM on mechanical properties

A number of possible mechanisms exists for the improved mechanical properties. Based on the experimental results and the CPFE model in the current study, one possibility explanation is discussed

here. The cumulative strain field of the three zones is plotted in Fig. 13. Sample areas were taken within the three zones, to avoid the effect at the interface of the neighbour zones. Strain accumulation at the lath interfaces was observed in the solidified melt pool and the transition zone. Strain accumulation sites were seen at the grain boundaries, lath interfaces and the triple points in the melt pool, see Fig. 13a. The martensitic  $\alpha$  laths in the surface layers display a high level of stress. In the transition zone, strain accumulates mainly within the  $\alpha$  phase, where the laths initiate. The original microstructure also showed grain boundary stress concentration (Fig. 13c), however, the stress within the equiaxed grain is more homogeneous compared with the melt pool and the transition zone. Compared with the FGM, the strain accumulation in the original microstructure does not show a gradient at the surface.

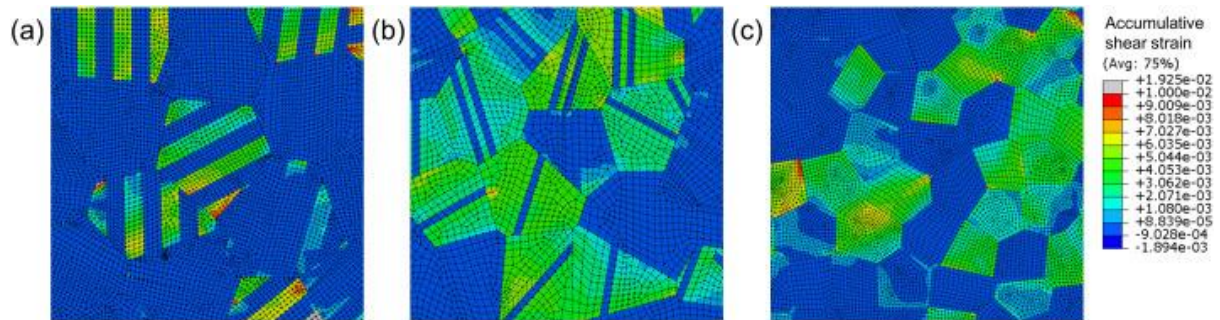


Fig. 13. Cumulative shear strain in the (a) surface martensitic, (b) transition, and (c) original microstructure zones.

The cumulative strain histogram, fitted with a normal distribution model, taken from the three zones are shown in Fig. 14. Due to high density of grain boundaries, high strain accumulation was observed in both the surface and the transition layer. The strain accumulation in the surface and transition zones therefore results in lower strain in the centre of the FGM sample, than would otherwise occur in the original microstructure. Wider distribution lines in the martensitic surface layer and transition zone indicate the existence of both high and low strain accumulation sites. This was mainly due to the high density of hard martensitic grain boundaries.

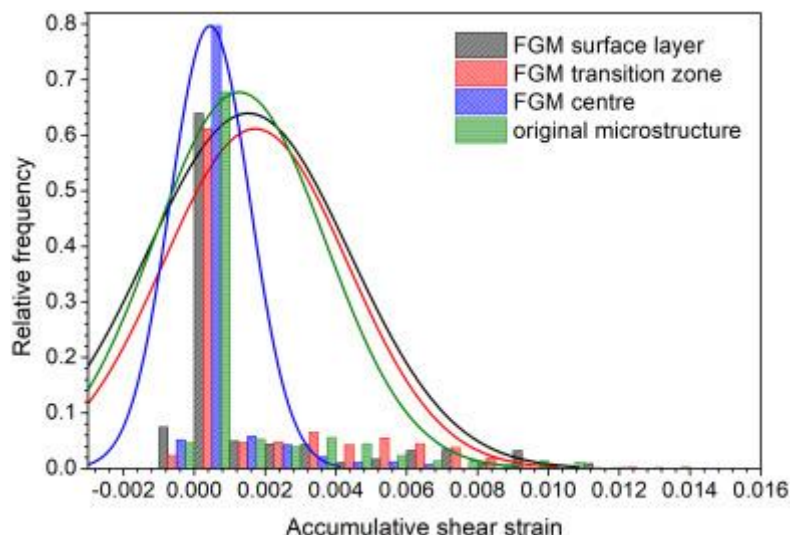


Fig. 14. Cumulative shear strain of original microstructure and laser treated FGM, as determined from the CPFE model.

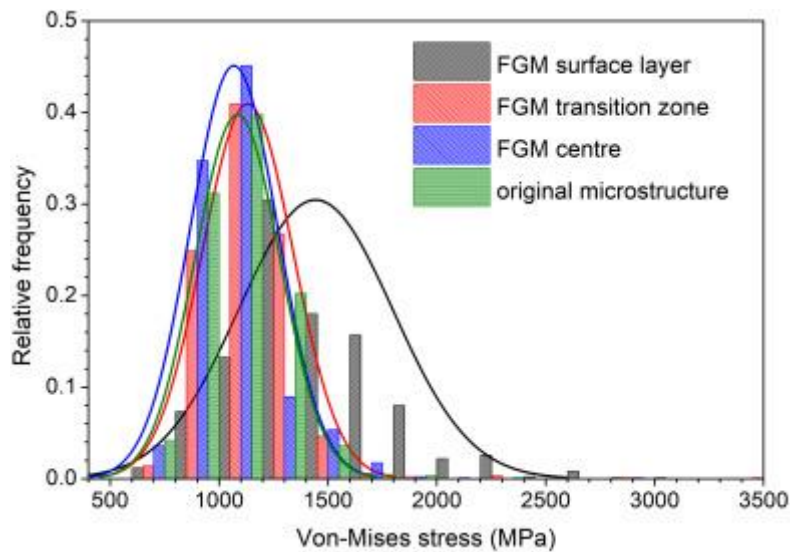


Fig. 15. Von Mises stress distribution of original microstructure and laser treated FGM from CPFE model.

## 5. Conclusions

High speed and high power laser modification was conducted on the surface of Ti6Al4V in the current study. A three zone microstructure with a martensitic layer, a transition layer, and the original microstructure was obtained. A CPFE model was developed to predict the tensile behaviour of the three zone model and the slip induced hardening of the surface layer was examined. To conclude, the major contributions of this work were:

High power laser treatment was conducted on Ti6Al4V samples with nine combinations of laser power and sample travel speed. A three zone gradient microstructure was obtained. A fully martensitic surface layer was resulted from the ultra-high cooling rate during the laser treatment. The transition zone was observed below the transition layer, which consists of the original  $\beta$  grain boundaries, and intragranular laths within equiaxed grains.

2) Crystal plasticity finite element simulation was performed. The mechanical properties of the three-stage microstructure were predicted. The input modulus was obtained from nanoindentation for the surface zone, grains boundary  $\beta$ , and original  $\alpha$  phase.

3) The present study provides a possible explanation to the hardening mechanism of LSM on Ti6Al4V. The original equiaxed microstructure results in high strain along the maximum in-plane shear stress (45 degree) direction. The surface zone prevented the propagation of continuous slip bands. On the other hand, the transition zone limited stress concentrations and potential delamination between the martensitic surface and the equiaxed microstructure at the centre of the samples.

## References

- [1] M. Naebe, K. Shirvanimoghaddam, Functionally graded materials: a review of fabrication and properties, *Appl. Mater. Today*, 5 (Supplement C) (2016), pp. 223-245
- [2] S. Ali, B. Ardeshir, Optimum Functionally Gradient Materials for Dental Implant Using Simulated Annealing, INTECH Open Access Publisher (2012)
- [3] L. Hao, J. Lawrence, *Laser Surface Treatment of Bio-implant Materials*, Wiley Online Library (2005)

- [4] A. Kurella, N.B. Dahotre, Review paper: surface modification for bioimplants: the role of laser surface engineering, *J. Biomater. Appl.*, 20 (1) (2005), pp. 5-50
- [5] T.H. Fang, et al., Revealing extraordinary intrinsic tensile plasticity in gradient nano-grained copper *Science*, 331 (6024) (2011), pp. 1587-1590
- [6] K. Lu, Making strong nanomaterials ductile with gradients, *Science*, 345 (6203) (2014), pp. 1455-1456
- [7] Q. Yang, et al., Effect of different surface asperities and surface hardness induced by shot-peening on the fretting wear behavior of Ti-6Al-4V *Surf. Coat. Technol.*, 349 (2018), pp. 1098-1106
- [8] Q. Wu, et al., Effect of shot peening on surface residual stress distribution of SiCp/2024Al, *Compos. Part B*, 154 (2018), pp. 382-387
- [9] Z. Cheng, et al., Extra strengthening and work hardening in gradient nanotwinned metals, *Science* (6414) (2018), p. 362
- [10] S. Katayama, et al., Surface Hardening of Titanium by Laser Nitriding, 1983(2) (1983), pp. 127-134
- [11] E. Chikarakara, et al., In vitro fibroblast and pre-osteoblastic cellular responses on laser surface modified Ti-6Al-4V, *Biomed. Mater.*, 10 (1) (2014), Article 015007
- [12] G. Lütjering, J.C. Williams, *Titanium*, Springer, Berlin; New York (2010)
- [13] G. Lütjering, Influence of processing on microstructure and mechanical properties of ( $\alpha$ + $\beta$ ) titanium alloys, *Mater. Sci. Eng. A*, 243 (1) (1998), pp. 32-45
- [14] S. Malinov, et al. Differential scanning calorimetry study and computer modeling of  $\beta \Rightarrow \alpha$  phase transformation in a Ti-6Al-4V alloy *Metall. Mater. Trans. A*, 32 (4) (2001), pp. 879-887
- [15] M. Kahlin, H. Ansell, J.J. Moverare, Fatigue behaviour of additive manufactured Ti6Al4V, with as-built surfaces, exposed to variable amplitude loading, *Int. J. Fatigue*, 103 (Supplement C) (2017), pp. 353-362
- [16] T. Dick, S. Basseville, G. Cailletaud, Fatigue modelling in fretting contact with a crystal plasticity model, *Comput. Mater. Sci.*, 43 (1) (2008), pp. 36-42
- [17] S. Khan, Analysis of tribological applications of functionally graded materials in mobility engineering, *Int. J. Sci. Eng. Res.*, 6 (2015), pp. 1150-1161
- [18] S. Yerramareddy, S. Bahadur, The effect of laser surface treatments on the tribological behavior of Ti-6Al-4V, *Wear*, 157 (2) (1992), pp. 245-262
- [19] R. Pederson, *Microstructure and Phase Transformation of Ti-6Al-4V*, Luleå tekniska universitet (2002)
- [20] A. Sandoval Amador, et al., Corrosion of Ti6Al4V ELI Surfaces Textured by CO2 Laser (2017)
- [21] A. Khorram, A. Davoodi Jamaloei, A. Jafari, Surface transformation hardening of Ti-5Al-2.5Sn alloy by pulsed Nd:YAG laser: an experimental study, *Int. J. Adv. Manuf. Technol.*, 100 (9) (2019), pp. 3085-3099

- [22] P. Jiang, et al. Wear resistance of a laser surface alloyed Ti–6Al–4V alloy Surf. Coat. Technol., 130 (1) (2000), pp. 24-28
- [23] V.K. Balla, et al. Microstructure, mechanical and wear properties of laser surface melted Ti6Al4V alloy, J. Mech. Behav. Biomed. Mater., 32 (2014), pp. 335-344
- [24] E. Chikarakara, Laser Surface Modification of Biomedical Alloys, (2012)
- [25] E. Chikarakara, S. Naher, D. Brabazon, High speed laser surface modification of Ti–6Al–4V Surf. Coat. Technol., 206 (14) (2012), pp. 3223-3229
- [26] P.J. Ashton, et al., The effect of the beta phase on the micromechanical response of dual-phase titanium alloys Int. J. Fatigue, 100 (2017), pp. 377-387
- [27] T.B. Britton, et al. The Effect of Crystal Orientation on the Indentation Response of Commercially Pure Titanium: Experiments and Simulations 466 (2010), pp. 695-719 (2115)
- [28] Z. Li, F. Yang Grain rotations during uniaxial deformation of gradient nano-grained metals using crystal plasticity finite element simulations Extreme Mech. Lett., 16 (2017), pp. 41-48
- [29] Z.-H. Wu, et al. Crystal plasticity finite-element simulation of Ti-6Al-4V alloy with 3D polycrystalline models 2nd Annual International Conference on Advanced Material Engineering (AME 2016), Atlantis Press (2016)
- [30] Z. Teng, et al. Micro–macro wear–fatigue of modular hip implant taper-lock coupling J. Strain Anal. Eng. Des., 49 (1) (2013), pp. 2-18
- [31] T. Dick, G. Cailletaud, Fretting modelling with a crystal plasticity model of Ti6Al4V Comput. Mater. Sci., 38 (1) (2006), pp. 113-125
- [32] Y. Huang, A User-material Subroutine Incorporating Single Crystal Plasticity in the ABAQUS Finite Element Program, Harvard Univ (1991)
- [33] F. Roters, et al., DAMASK – the Düsseldorf Advanced Material Simulation Kit for modeling multi-physics crystal plasticity, thermal, and damage phenomena from the single crystal up to the component scale Comput. Mater. Sci., 158 (2019), pp. 420-478
- [34] F. Roters, et al. Overview of constitutive laws, kinematics, homogenization and multiscale methods in crystal plasticity finite-element modeling: theory, experiments, applications Acta Mater., 58 (4) (2010), pp. 1152-1211
- [35] M. Yaghoobi, et al. PRISMS-Plasticity: an open-source crystal plasticity finite element software Comput. Mater. Sci., 169 (2019)
- [36] L.-C. Zhang, L.-Y. Chen, L. Wang, Surface Modification of Titanium and Titanium Alloys: Technologies, Developments, and Future Interests, 22 (2020), p. 1901258 (5)
- [37] I. Watanabe, et al., Laser surface treatment to improve mechanical properties of cast titanium Dent. Mater., 25 (5) (2009), pp. 629-633
- [38] L. Ladani, et al. Effect of varying test parameters on elastic–plastic properties extracted by nanoindentation tests, Exp. Mech., 53 (8) (2013), pp. 1299-1309
- [39] E. Harvey, L. Ladani, M. Weaver, Complete mechanical characterization of nanocrystalline Al–Mg alloy using nanoindentation, Mech. Mater., 52 (2012), pp. 1-11

- [40] Y. Geng, N. Harrison, Functionally graded bimodal Ti6Al4V fabricated by powder bed fusion additive manufacturing: crystal plasticity finite element modelling, *Mater. Sci. Eng. A* (2019), p. 138736
- [41] A.C. Magee, L. Ladani Representation of a microstructure with bimodal grain size distribution through crystal plasticity and cohesive interface modelling *Mech. Mater.*, 82 (2015), pp. 1-12
- [42] C. Fizanne-Michel, et al. Determination of Hardness and Elastic Modulus Inverse Pole Figures of a Polycrystalline Commercially Pure Titanium by Coupling Nanoindentation and EBSD Techniques 613 (2014), pp. 159-162
- [43] S.F. Choudhury, L. Ladani, Single crystal plasticity finite element analysis of Cu6Sn5 intermetallic, *Metall. Mater. Trans. A*, 46 (3) (2015), pp. 1108-1118
- [44] J.L.J.T. Bassani, *Microstructures, Hardening of FCC Crystals Undergoing Multiple Slip* (1970), p. 14
- [45] J.L. Bassani, Hardening of FCC crystals undergoing multiple slip, *Textures Microstruct.*, 14 (1991), pp. 1097-1102
- [46], Y. Fang, et al. Influence of SiC fiber on thermal cycling lifetime of SiC fibers/YSZ thermal barrier coatings by atmospheric plasma spraying, *Ceram. Int.*, 44 (15) (2018), pp. 18285-18293
- [47] J.W. Hutchinson, Bounds and self-consistent estimates for creep of polycrystalline materials, *Proceedings of the Royal Society of London. A. Mathematical and Physical Sciences*, 348 (1976), pp. 101-127, 1652